



Research Article

Copyright © All rights are reserved by Farid Abu Shammala

Facile Fabrication of a Low-Cost Lignosulfonate–Graphene Oxide–Polyaniline Ternary Nanocomposite for the Highly Efficient Removal of Pb(II) and Cr(VI) Ions from Aqueous Solutions

Farid Abu Shammala*

Department of Chemistry, University of Palestine, Palestine

*Corresponding author: Farid Abu Shammala, Faculty of Pharmacy, Department of Analytical Chemistry, University of Palestine, El-Zahra City, Gaza, Palestine.

Received Date: June 05,2020

Published Date: June 23,2020

Abstract

In this study, we demonstrate a one-step method for fabricating a novel lignosulfonate–graphene oxide–polyaniline (LS-GO-PANI) nanocomposite aerogel, were prepared and employed for adsorption and removal of (Pb(II)) and Cr(VI) ions from aqueous solution. The results have shown that (LS-GO-PANI) nanocomposite exhibits a very high affinity and selectivity towards Pb(II) and Cr(VI) ions. The morphology and structure of the LS-GO-PANI ternary nanocomposite were characterized by using transmission electron microscopy (TEM), scanning electron microscopy (SEM), atomic force microscope (AFM), fourier-transform infrared spectroscopy (FTIR), Raman spectroscopy, X-ray diffraction spectroscopy (XRD), and X-ray photoelectron spectroscopy (XPS). Furthermore, the effects of adsorption time, initial pH value, adsorbent concentration, and initial adsorbate concentration on the adsorption of Pb(II) ions in aqueous solution were investigated by batch experiments. The LS-GO-PANI ternary nanocomposite showed an adsorption capacity as high as 356.4 mg g⁻¹ for Pb(II) ions and 282.15 mg/g mg/g for Cr(VI) ions at 30 °C. Moreover, the adsorption kinetic and equilibrium data were described well with the pseudo-second-order and Langmuir isotherm models for the Pb(II) and Cr(VI) ions adsorption process. The results showed that the LS-GO-PANI ternary nanocomposite has broad application potential in treating Pb(II) and Cr(VI) ions containing industrial wastewater.

Keywords: Graphene oxide; Lignosulfonate; Polyaniline; Heavy metals; Nanocomposites; Adsorption

Introduction

The indiscriminate disposal of non-biodegradable heavy metals waste have received a paramount attention to environmental chemists due to their toxic nature. Heavy metals are usually present in trace amounts in natural waters but many of them are toxic even at very low concentrations. Human activities have been found to the major contribute to environmental heavy metals pollution due to the everyday manufacturing of goods to meet the demands of the large population. The most common heavy metals are lead Pb(II) ions, generated from both natural and anthropogenic sources. Lead is widely used as a raw material in industrial production.

Lead ions Pb(II) are often found in lead dyes, refineries, pulp industries, storage batteries, lead ore smelting, and recycled lead industrial wastewater [1]. The presence of Pb(II) in wastewater can be absorbed and enriched by aquatic animals and plants and then enter the human body through the food chain, thereby posing serious damage to the nerves system, cause mental decline, behavioral abnormalities, damage digestive systems, kidneys, and endocrine systems of the humans [2-5]. Therefore, new methods must be developed for effective and selective removing of (Pb(II)) and Cr(VI) ions from wastewater. Another toxic heavy metal pollutant

is Chromium Cr(VI), chromium found in two oxidation states, III and VI. As compared to the III oxidation state, VI oxidation state of chromium is considered more toxic. Cr(VI) present mainly in the effluents of electroplating, leather tanning, textile industries, metal finishing, and chromate preparations [6]. World Health Organization (WHO) guideline for Cr(VI) in drinking water is $50 \mu\text{g L}^{-1}$ [6]. Exposure to elevated levels of Cr(VI) could lead to gastrointestinal disorders, liver, kidney and lung cancer, cardiovascular shocks, and other health related problems [6].

Indeed, most of the physical and chemical technologies for Pb(II) and Cr(VI) ions adsorption remediation are not economically feasible, require handling of large amounts of sludge, which destroys the surrounding ecosystems and are very expensive. Therefore, it is necessary to investigate low-cost, effective alternatives. Adsorption is regarded as the most effective and economically viable option for the removal of heavy metal ions from aqueous solution. Carbon-based materials with porous structures find extensive use in many fields such as adsorption, separations, super capacitors, drug delivery, lithium ion batteries and sensing due to their distinctive properties [7-13]. Previously, activated carbon is a highly effective alternative used for the adsorption of heavy metals from wastewater, but it is soluble under extremely acidic conditions [14]. It is only feasible for very dilute solutions, is labor intensive because it requires frequent regeneration and it is not selective in terms of metal attenuation [15]. Indeed, many synthesized materials, such as one-dimensional (1D) nanofibers [16,17], two-dimensional (2D) films or membranes [18,19], and three-dimensional (3D) scaffolds [20-22], have been utilized as effective absorbents for treating Pb_2+ -containing water systems. 1D and 2D nano-adsorbents have a high adsorption capacity and adsorption rate for Pb^{2+} due to their high specific surface area and chemical activity, but the preparation of these nanomaterials usually requires stringent conditions, such as a high temperature, high pressure, high purity reagents, etc. In addition, these nano-adsorbent materials are difficult to recollect because of their small size. Macroscopic 3D porous material can overcome the above shortcomings. It not only provides a high surface area, but also facilitates solid-liquid separation. To achieve an economical use of the synthesized absorbents, an important aspect is to find low-cost and source-rich natural materials for fabricating various functional nanomaterials [23,24].

Lignosulfonates, are water-soluble anionic polyelectrolyte polymers, are byproducts from the production of wood pulp using sulfite pulping [25]. Lignosulfonates have a wide variety of applications such as plasticizers in making concrete, production of plasterboard, disperse pesticides, dyes, carbon black, tanning leather. They are also used to suppress dust on unpaved roads, and used as binders in well-paper, particle boards, linoleum flooring, coal briquettes, and roads [25]. This molecule contains a large amount of sulfate, carboxyl and hydroxyl functional groups that can complex metal ions [26]. Therefore, sodium alginate can also be used as a medical antidote for treating heavy metal ion poisoning [27]. However,

alginate aerogels have poor mechanical properties. After repeated use, the aerogel structure can be easily destroyed, thereby resulting in an unstable adsorption capacity for heavy metal ions [28]. This kind of material shows improved mechanical properties given its special adhesion. In addition, Polyaniline (PANI) is a conducting polymer of the semi-flexible rod polymer family. The major applications are printed circuit board manufacturing: final finishes, antistatic and ESD coatings, and corrosion protection [29]. Polyaniline and its derivatives are also used as the precursor for the production of N-doped carbon materials through high-temperature heat treatment [30]. Polyaniline with two types of functional groups (sulfonated poly(aniline-co-o-aminophenol), s-copolymer) has been prepared by the electrochemical copolymerization of aniline and o-aminophenol in sulfuric acid solution followed by sulfonation of the copolymer in the concentrated sulfuric acid [30].

In this work, we synthesized new nanohybrid materials composed of graphene oxide (GO), lignosulfonate, and polyaniline (LS-GO-PANI) nanocomposite to fully eliminate the Pb(II) and Cr(VI) ions from aqueous solutions under different experimental conditions. The innovative nanohybrid nanomaterial was characterized by different techniques. Optimum conditions, dynamics, and thermodynamics for the eradication of the Pb(II) and Cr(VI) ions were also investigated.

Experimental

Reagents and chemicals

All the chemical used in this study were prepared from Sigma Aldrich (St. Louis, Mo, USA) and Merck (KGaA, Darmstadt, Germany) and used without modification and without further purification. Natural graphite powder (325 mesh, purity of 99.95%), lignosulfonate (low viscosity, LS, $\text{C}_{20}\text{H}_{24}\text{Na}_2\text{O}_{10}\text{S}_2$, MW 534.51), vitamin C (VC, purity of 99.5%), polyaniline, nitric acid (HNO_3), sodium hydroxide (NaOH), metal salts, $\text{Pb}(\text{NO}_3)_2$, $\text{K}_2\text{Cr}_2\text{O}_7$, and other reagents were of analytical grade. The experimental Pb(II) and Cr(VI) solutions was prepared by dissolving $\text{Pb}(\text{NO}_3)_2$ and $\text{K}_2\text{Cr}_2\text{O}_7$ in deionized water, respectively. All metal salt solutions were prepared by using ultrapure water. The pH value of the solution was adjusted with 1.0 M HNO_3 or NaOH.

Instrumentation measurements

FT-IR spectra were conducted on a Vertex 70 instrument (Bruker, Rheinstetten, Germany) at a resolution of 0.5 cm^{-1} , and in the range of 500 cm^{-1} to 4000 cm^{-1} . The atomic force microscope (AFM, Nanoscope III Veeco Co. Ltd., Santa Barbara, USA) was obtained to characterize the GO samples. Samples for AFM analysis were prepared on freshly cleaved mica. The X-ray diffraction (XRD) patterns of dried samples were measured with a Bruker D8 Advance diffractometer. The conditions of test were: the tube current and voltage at 20 mA and 30 kV, respectively, Cu target ($\lambda = 0.15418 \text{ nm}$), and data were collected from the 2θ angular regions between 5° and 60° . The thermal stability of the dried samples was em-

ployed investigated using a TGA Q500 (TA Instruments, New Castle DE, USA). The samples were heated in an aluminum crucible to 650 °C at a heating rate of 20 °C/min. Surface morphology of dried samples was analyzed by scanning electron microscopy (SEM; Bruker) at 10 kV. The samples for SEM analysis were coated with a thin layer of gold (2 nm) by sputtering to promote conductivity before SEM observation. To observe the nitrogen adsorption isotherms at -196 °C, ASAP 2460 instrument was employed. The specific surface area was evaluated from the adsorption branch of the isotherm using Brunauer-Emmett-Teller theory (BET). The X-ray photoelectron spectroscopy (XPS) was performed on a Axis Ultra DLD spectrometer (Kratos, Manchester, UK) with monochrome Al K α radiation ($h\nu = 1486.6$ eV). A JJ-1 electric agitator (Changzhou Guohua Company, Changzhou, China) and MS7-H550-Pro agitator (Dragon Laboratory Instruments Limited, Beijing, China) were used for mechanical and magnetic stirring, respectively. A PHS-3E acidity meter was used to determine the pH value of the solution. The concentration of Pb(II) and Cr(VI) after adsorption was measured using atomic absorption spectrophotometer (Z-2000, Hitachi Ltd., Tokyo, Japan).

Synthesis of graphene oxide

Graphene oxide (GO) was synthesized from natural graphite powder according to the procedures described by Hummers's method (Hummers and Offeman 2002). In order to avoid aggregation of the GO during drying process, the GO sample was obtained first by freeze-drying. Then dried GO sample was dispersed in water by using ultrasonication for 1 h to get an aqueous dispersion at a concentration of 2.0 mg/mL. were prepared.

Synthesis of the nanocomposite (LS-GO-PANI)

The adsorbent (LS-GO-PANI) was prepared as follows. First, 2.0 g of alginosulfate was weighed and dissolved in 98.0 mL of ultrapure water. Second, VC (20 g), and GO aqueous dispersion (200 mL) were added to a 500 mL glass flask. The reaction mixture was stirred at room temperature until it became a stable suspension. The aqueous dispersions of the LS, VC, and GO were then heated at 60 °C, the solution and mechanically stirred for 3 hours. Third, 2.0 g of polyaniline was added to the mixture, and stirring was continued for 12 hours at room temperature, and the ternary nanocomposite were then collected by filtration and washed thrice with ultrapure water. Fourth, the hydrogels were immersed in ultrapure water, placed in a vacuum freeze-drying apparatus, frozen for 4 hours, and vacuum dried for 20 hours to obtain the lignosulfonate-graphene oxide-polyaniline (LS-GO-PANI) nanocomposite aerogel.

Adsorption and desorption tests

In an adsorption experiment, About 100 mg of LS-GO-PANI nanocomposite was weighed and added to 100 mL of the 0.1 mM of Pb(II) or Cr(VI) solution, loaded in a 200 mL conical flask and placed it in an air table with 200 rpm stirring speed at 25 °C for 24 hours to reach equilibrium. The desired pH value was adjust-

ed using 0.1 M HCl or 0.1 M NaOH solution and eventually filtered through filter paper and a funnel at atmospheric pressure. The amount of Pb(II) or Cr(VI) remaining in the filtrate was measured using the atomic absorption spectrophotometer. In a desorption experiment, Pb(II) or Cr(VI) loaded LS-GO-PANI nanocomposite was immersed in 50 mL of the 0.05 M HNO₃ solution for 30 minutes, filtered, and washed thrice with ultrapure water, and the amount of Pb(II) or Cr(VI) in the eluate was then determined using atomic absorption spectrophotometer.

Results and Discussion

TEM images

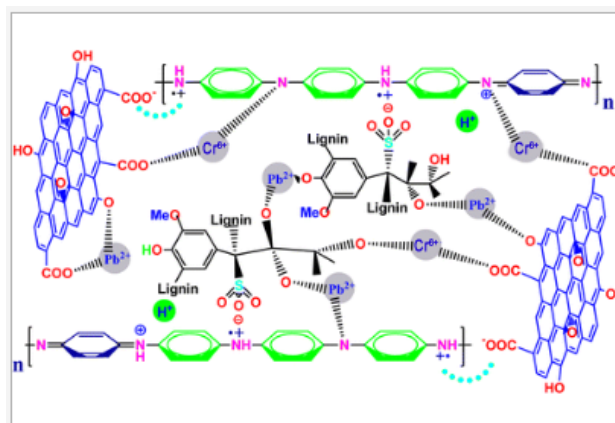


Diagram 1:

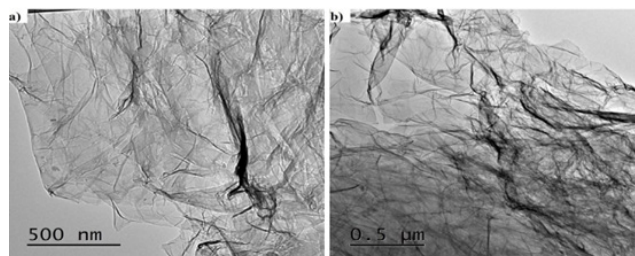


Figure 1: TEM images of (a) graphene oxide (GO), (b) lignosulfonate-graphene oxide-polyaniline (LS-GO-PANI) nanocomposite.

The morphologies and structures of GO and LS-GO-PANI nanocomposite were observed by TEM and SEM, respectively. TEM images of nano-graphene oxide (GO) (Figure 1-a), and graphite oxide with LS-GO-PANI nanocomposite are illustrated (Figure 1-b). The specific surface area values of GO and LS-GO-PANI were examined by BET analysis (Brunauer-Emmett-Teller) and the results are shown that the values of the specific surface area and the pore size of the GO were 64.32 m² g⁻¹ and 0.2392 cm³ g⁻¹, respectively. The values of specific surface area and the pores size of the LGPH were 110.44 m² g⁻¹ and 0.2839 cm³ g⁻¹, respectively [31-33]. The BET surface area of LS-GO-PANI is larger than GO due to the surface of LS-GO-PANI being rougher than MGO, after GO was modified using LS and PANI which is also seen in the TEM images for GO and LS-

GO-PANI (Figure 1). As the figures indicate, graphene oxide has a plate structure and the LS and PANI are penetrated and spread over the graphene oxide plates (Figure 1).

SEM images

Figure 2a–b depicts the SEM images of GO and LS-GO-PANI, the morphology and microstructure of monolith were analyzed by scanning electron microscopy (SEM-S420, HITACHI) equipped with a field-emission electron gun. The SEM image of GO (Figure 2a) depicts a typical flake-like morphology, agglomerated into a two-dimensional multilayered structure with a smooth surface and lateral sizes of several nanometers, which demonstrates the large specific surface area of GO. The diverse layers can overlap and interweave with each other to form the bright and shaded areas on the GO surface. In Figure 2b, SEM images of the LS-GO-PANI nanocomposites are showcased. A much rougher surface and more wrinkled structure are found in the LS-GO-PANI image, and yet, the image was very similar to the GO SEM image. The cross-sectional analysis showed that the thickness of the GO sheets were in the ranges of 0.98 nm, which illustrated that the GO sheet was about one-atom-thick graphene oxide. SEM images results of freeze-dried samples of LS-GO-PANI indicated a well-defined and interconnected 3D porous network as revealed by. It is depicted that PANI and LS assemble on the surface of GO sheets. The π - π stacking of GO sheets plays an important role in the formation 3D network porous structure. SEM analysis exhibited formation of interconnected 3D morphology and it can be noted that incorporation of LS and PANI with GO brought significant change in pore wall thickness and shrinkage in average size compared to those of GO. High magnification SEM image of hybrid samples showed the presence of needle-like LS and PANI in random direction which behave as compact skeleton within the dense and wrinkling type graphene sheets. Thus, it can be inferred that these surface decorated/adsorbed LS and PANI may promote

roughness between adjacent graphene sheets that results in compact 3D assembly due to strong chemical interaction. Furthermore, the results of the LS-GO-PANI nanocomposite indicates the π - π conjugation and hydrogen bonding between graphene sheets and LS and PANI contributed to the successful construction of 3D porous structure [33-35]. Thus, favoring the accumulation and adsorption of Pb(II) and Cr(VI) ions from aqueous samples. Moreover, the multilevel pore structure of LS-GO-PANI provided large specific surface area (473.5 m²/g) that was higher than that of GO (261.7 m²/g). These findings were also confirmed by the nitrogen adsorption-desorption isotherms (Figure 2).

Elemental analysis and mapping of phases

The elemental distribution mapping performed in order to find different elements and their distribution in the synthesized samples, energy dispersive X-ray (EDX) analysis was accomplished as seen in Figure 3. The EDX spectrum of GO shows C and O as the main component while the composite materials showcase all the elements of GO, PANI and LS, including C, O, S and N. The % weight of N and O atoms, respectively, decreases and increases with an increasing GO percentage. The presence of a high amount of S in the synthesized samples suggests effective incorporation of the LS in the structure of the nanocomposite. Consequently, the results indicated that the specific surface area of LS-GO-PANI was larger than that of GO, improving the adsorption capacity to metal ion. Thus, the large surface area of LS-GO-PANI contributes to the high adsorption capacity during the hydrothermal reaction. LS and PANI incorporated into graphene sheets through both covalent and non-covalent interactions, such as π - π conjugation and hydrogen bonding. The negatively charged LS molecules spread in the interlayer of graphene oxide sheets, thus prevents the restacking of graphene sheets through electrostatic repulsion (Figure 3).

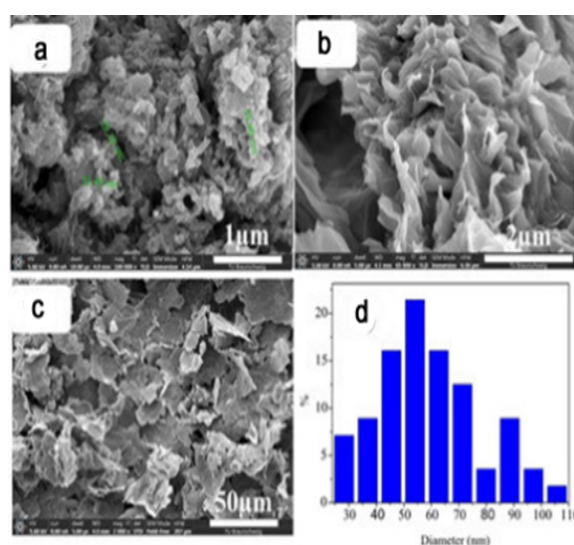


Figure 2: SEM images of (a) Graphite oxide (GO), (b, c) graphite oxide with lignosulfonate and polyaniline nanocomposite LS-GO-PANI (d) particle size distribution histogram of LS-GO-PANI.

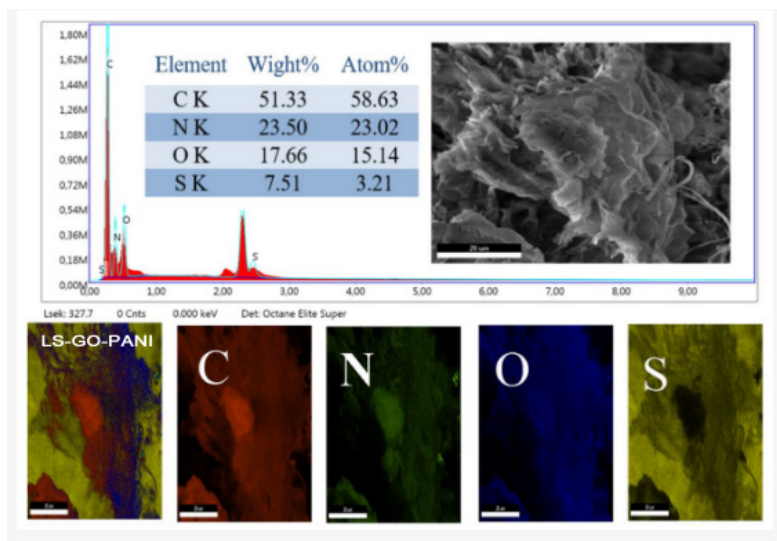


Figure 3: Elemental analysis and mapping of LS-GO-PANI -nanocomposite.

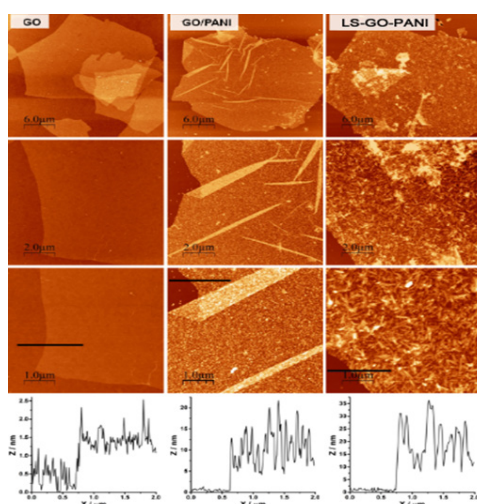


Figure 4: AFM images of GO, GO-LS and LS-GO-PANI nanocomposites at different scan sizes (30, 10 and 5 μm), and height profiles (thicknesses) (for the 5 μm scan size images) nanoplatelets measured from AFM image.

AFM image and thickness

Atomic force microscope was performed to examine the in three-dimensional topography of our samples, and to provides various types of surface measurements. Figure 4 shows the morphology and thickness of LS-GO-PANI nanocomposite by AFM. Figure 4 shows that LS-GO-PANI nanocomposite samples typically had flake-like and sheet-like structures with less than 1 μm lateral size and the range of thickness of LGPH samples was between 1 to 3 nm. The layer-to-layer distance (d-spacing) of graphene oxide (GO) is 0.850 nm, which indicated that this LS-GO-PANI nanocomposite sample typically has 1 to 3 layers. The lateral size of LGPH was typically less than 1 μm , which was less than that of graphene oxide (GO) made from natural graphene. The sonication can exfoliate the LS-GO-PANI to fewer layers, and the nanoscaled LS-GO-PANI nanocomposite may apply for conductive materials (Figure 4).

FTIR images

FTIR spectra of the different samples have been recorded as presented in Figure 5 a and b. The successful oxidation of graphene oxide was confirmed in Figure 4a, by the presence of various kinds of oxygen functionality such as peak at 3129-3440 cm^{-1} which are mainly originated from the stretching vibration of hydroxyl group (-OH). The peaks attributed to the deformation vibration of the tertiary (C-OH) groups appeared at 1400 cm^{-1} . The peaks at 1598 cm^{-1} for carboxylic group (-C=O), the bands located at 1620-1630 cm^{-1} resulted from the (C=C) stretching mode of the graphitic domains. The peaks located at approximately 1225 and 1080 cm^{-1} correspond to the stretching vibrations of (C-O-C) and (C-O), respectively. The peaks at 1218 cm^{-1} for epoxy (C-O) stretching and alkoxy (C-OH) stretching at 1043 cm^{-1} . The peaks located at approximately 1225 and 1080 cm^{-1} correspond to the stretching vibrations of

(C-O-C) and (C-O), respectively. In addition, the peaks attributed to the deformation vibration of the tertiary C-OH groups appeared at 1400 cm^{-1} . These hydrophilic groups on the surface are very important to improve the interaction between LS, PANI and GO sheets. As shown in Figure 4b the FT-IR spectra of LS-GO-PANI nanocomposites, the peak at $3440\text{--}3129\text{ cm}^{-1}$ was due to the O-H stretching. The bands around $1350\text{--}1342\text{ cm}^{-1}$ are attributed to sulfonic acid groups. The bands between 839 and 608 cm^{-1} was due to the C-S stretching vibration. The characteristic peaks at 3213 cm^{-1} and 1598 cm^{-1} belonging to GO can also be observed in the spectra of GO and LS-GO-PANI. Interestingly, spectra in Figure 3b showed shifting of the functional groups such as carboxyl band (C=O) from 1721 cm^{-1} to carboxylic stretching 1727 cm^{-1} which confirmed the successful reaction between GO, LS and PANI after treatment. This indicated that there exist a certain number of functional groups on reduced GO sheets. The characteristic peaks at 1635 and 1567 cm^{-1} are attributed to the stretching vibration of quinoid and benzenoid rings on PANI molecular chain. The characteristic peak at 1417 cm^{-1} is corresponding to the stretching mode of N-Q-N where Q represents the benzenoid ring. Additionally, compared with the GO, the S=O symmetric stretching at 1023 cm^{-1} belonging to LS was also observed, which indicated the proposed formation of LGPH. The existences of sulfonic acid groups was evident from the FTIR spectra and these groups were responsible for improving its adsorption capacity to water and metal ions. The change at $3129\text{--}3440\text{ cm}^{-1}$ could be ascribed to the strong interaction through hydrogen bonds and π - π conjugation between LS and GO sheets. This phenomenon is suggesting that the presence of LS and PANI plays important role for the self-assembly of monolithic material and promotes chemical interaction force, presumably, hydrogen bonding as evident

from shifting of these functional groups, since we failed to obtain 3D monolith in the absence of LS and PANI. However, nature of hydrogen bonding between bare graphene sheets and/or between GO sheets and LS follows different routes. Compared to control sample, hybrid spectrum exhibits downshifting at starching vibration of hydroxyl (OH), carboxyl (C-O, C-O-C), and N-H bending vibration mode. This shift can be seen as synergy effect of strong hydrogen bonding between graphene sheets and LS, thus greatly influencing the microstructure morphology and mechanical and thermal properties of hybrid material. It can be inferred that strong chemical interaction between GO, PANI and LS is predominantly influenced by C=O...HO and N-H...OH type hydrogen bonding during the hydrothermal treatment. Moreover, shrinkage in OH starching was due to deoxygenation of graphene (Figure 5).

Raman spectra

The structural characterisation of PANI, GO-PANI and LS-GO-PANI nanocomposites were performed by Raman spectroscopy, as presented in Figure 6. Raman bands in the spectra of PANI, GO/PANI and LS-GO-PANI at 632.8 nm excitation wavelength are mainly attributed to the polymer due to resonance effects with the polaronic/bipolaronic electronic transitions of PANI, and the high content of polymer in these materials. The spectra presented in Figure 6a show the characteristic features of the PANI polymer for all samples. However, comparing the spectra of the nanocomposites with the neat polymer (PANI), the bands at ca. 1336 and ca. 1600 cm^{-1} for the hybrid materials present higher relative intensities. These results can be attributed to the contribution of GO bands, and changes in the doping state of the polymer due to interaction with the LS and PANI components (Figure 6).

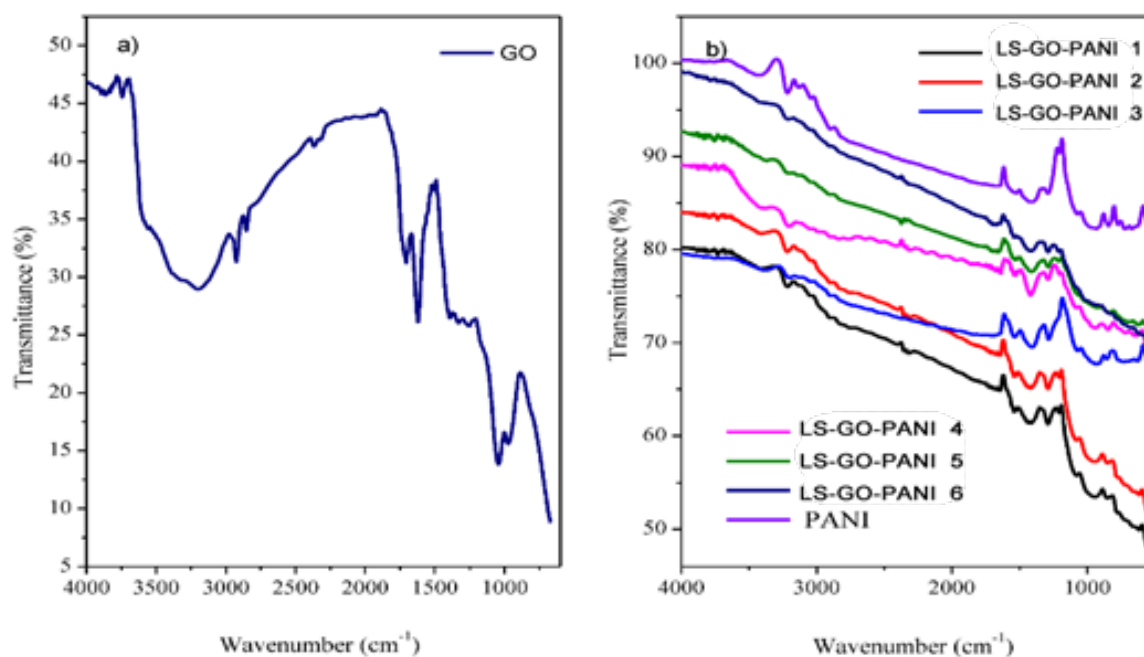


Figure 5: AFM images of GO, GO-LS and LS-GO-PANI nanocomposites at different scan sizes (30, 10 and $5\text{ }\mu\text{m}$), and height profiles (thicknesses) (for the $5\text{ }\mu\text{m}$ scan size images) nanoplatelets measured from AFM image.

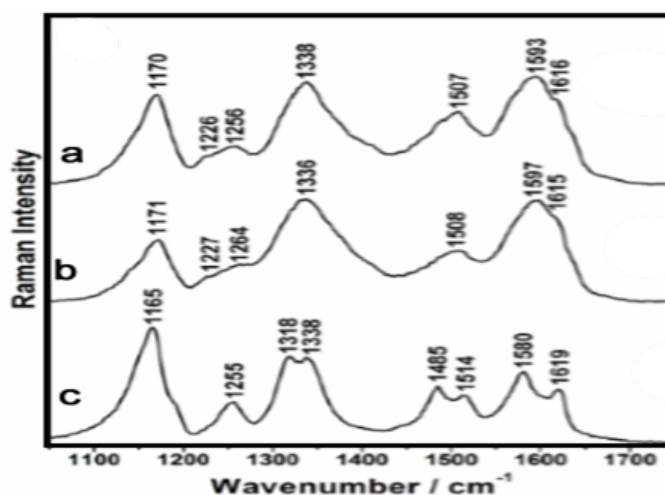


Figure 6: Raman spectra ($\lambda_0 = 632.8 \text{ nm}$) of (a) LS-GO-PANI, (b) GO/PANI and (c) PANI in the range of $1050\text{--}1750 \text{ cm}^{-1}$.

XRD patterns

Figure 7 XRD spectra of (a) GO, (b) lignosulfonate (LS), (c) PANI, and (d) LS-GO-PANI nanocomposite. The GO pattern (Figure 6a) showed a peak at $\sim 10.7^\circ$ corresponding to the (001) inter-planar spacing of 8.30 \AA which caused by the oxygen-rich groups on both sides of the sheets and the water molecules trapped between the GO sheets. The calculated interlayer spacing of the freeze-dried GO and LS-GO-PANI nanocomposite was observed to be 3.69 \AA , and 3.65 \AA , respectively. This value was much lower than that of GO (8.30 \AA), which suggested the presence of π - π stacking between graphene sheets in the composites and also the presence of a certain number of functional groups on reduced GO sheets. For GO spectra, the

reduced GO sheets can encapsulate water in the process of self-assembly due to the presence of residual hydrophilic oxygenated groups. For LS-GO-PANI, in addition to functional groups on reduced GO sheets, the hydrophilic groups of LS and PANI could also capture a multitude of water molecules. Because of this factor and the stacking of graphene sheets, the composites can be successfully synthesized by one-step method. Lignosulfonate (LS) XRD spectra shows a broad peak between 20° and 30° was attributed to its low graphitization and amorphous nature. Furthermore, there has been obvious distinction between the XRD patterns of GO, LS and LS-GO-PANI, which indicated that LS was chemically reacted on GO surface. Moreover, there has been obvious similarity between the XRD patterns of PANI and LS-GO-PANI nanocomposite (Figure 7).

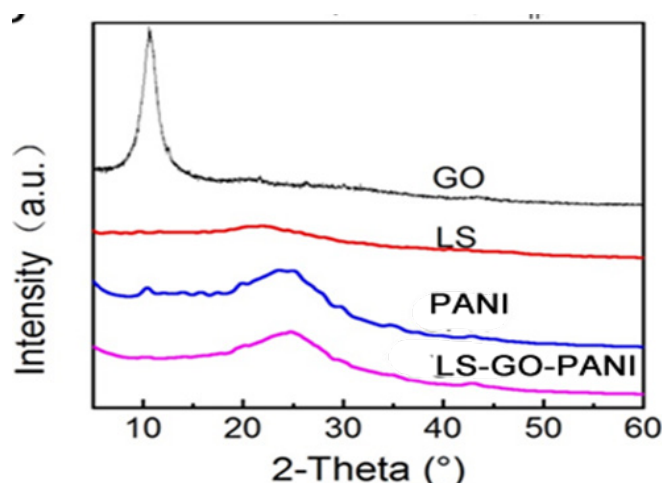


Figure 7: XRD spectra of (a)GO, (b) lignosulfonate (LS), (c) PANI, and (d) LS-GO-PANI nanocomposite.

XPS patterns

High-resolution XPS spectra can also provide information on the reduction degree of GO, since C 1s core level photoelectrons present slightly different binding energies depending on the envi-

ronment of the carbon atoms. Figure 8 shows the high-resolution XPS spectra at the C 1s core level for GO and rGO samples prepared by reactions at 25°C for 7 days and at 80°C for 3. XPS spectra of GO and rGO consist mainly of two asymmetric and highly overlapping peaks (maxima at ca. 285 and ca. 287 eV). The comparison

of these spectra clearly shows the increase of relative intensity of the low-binding energy peak upon reduction. This is attributed to the partial recovery of the sp²-hybridized carbons in the graphene structure, since pristine graphite presents only an asymmetric peak at ca. 284 eV (carbon atoms in sp² environment). The curve fitting of the C 1s spectra, also presented in Figure 8, can provide detailed information on the oxygen-containing groups, since these groups induce different environments for the carbon atoms and, consequently, their corresponding C 1s photoelectrons present slightly different binding energies. The comparison of the curve fitting for GO and rGO-25 shows the increase of the contribution from sp² carbons (C=C) and hydroxy groups (C-OH) upon reduction, and the decrease of sp³ carbons (C-C + C-H) and epoxy groups (C-O-C). These results are in good agreement with the literature and indicate the recovery of the sp² carbon atoms from the sp³ carbon atoms and epoxy groups, and the conversion of some epoxy to hydroxy groups [28,45,46,48]. In contrast, rGO presents a dramatic change in the C 1s spectral profile, evidenced by an intense peak at ca. 284 eV and a weak shoulder at 285–290 eV. The comparison of the curve fitting for this sample and rGO shows a significant increase of the contribution from the sp² carbon atoms and decrease of the contribution from sp³ carbon atoms, hydroxy and epoxy groups. These features are very similar to data reported in literature for chemically reduced GO [36-38] and indicate a high

degree of reduction of the rGO sample. This also points out the very important role of the temperature on the recovery of the sp² carbon network in graphene oxide (Figure 8).

Figure 9 shows XPS spectra at the N 1s core level of PANI, GO/PANI and LS-GO-PANI nanocomposite, and the respective curve fitting results. Analogously to C 1s, XPS spectra at the N 1s core level can be discussed in detail and provide interesting structural information on the GO/PANI and LS-GO-PANI nanocomposite. In the present work, the N 1s peaks are mostly from nitrogen-containing groups of PANI, the amine, imine or charged nitrogen sites of the polymeric chains. Therefore, XPS spectroscopy provides important information on the oxidation and doping states of the polymer in PANI-based materials. The N 1s peak of PANI-based materials is dominated by an amine (–NH–)-related component at ca. 399 eV, but also shows components of quinone (=N–), polaron (–N•+H–) and bipolaron (=N+H–) groups at ca. 398, ca. 401 and ca. 402 eV, respectively. The comparison of spectral data for PANI and rGO/PANI in Figure 9 indicate that PANI chains present a higher doping state in the presence of GO flakes. XPS data for the LS-GO-PANI nanocomposite clearly shows a significant increase in the relative intensity of the peak with higher binding energy. These results clearly indicate that LS nanoparticles also play an important role to the increase of the doping state of PANI (Figure 9).

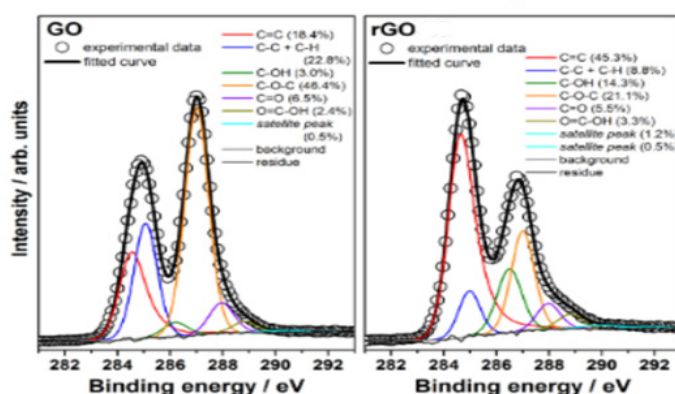


Figure 8: XPS spectra at the C 1s core level of GO and rGO samples prepared by reactions at 25 °C for 7 days or at 80 °C for 3 h.

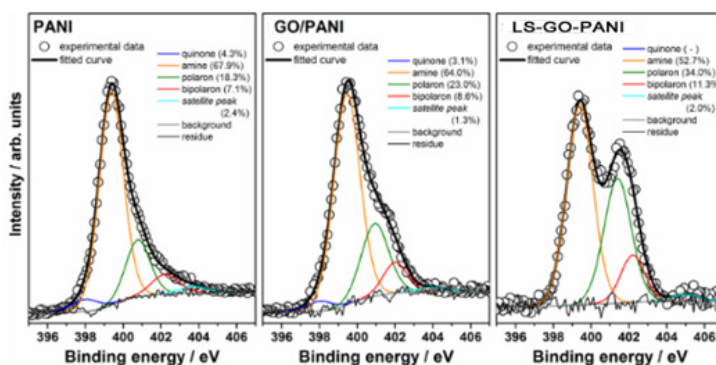


Figure 9: XPS spectra at N 1s core level of (a) PANI, (b) GO/PANI and (c) LS-GO-PANI nanocomposite.

Time profile and adsorbent dosage for Pb(II) and Cr(VI) ions on LS-GO-PANI nanocomposite

Figure 10a,b shows that the adsorption removal of Pb(II) and Cr(VI) with LS-GO-PANI nanocomposite was rapid and immediately (within 5 min) reached 99% maximum adsorptive removal of Pb(II) and Cr(VI). As the contact time further increased to 90 min, the adsorption percentage becomes constant. Therefore, the contact time can be optimized to 30 min for both Pb(II) and Cr(VI) with LS-GO-PANI nanocomposite, respectively. The effect of the adsorbent dosage (Figure 10c) on the adsorption of Pb(II) and Cr(VI) (10 mg L^{-1}) was studied by varying the dosage from 0.1 to 0.8 g L^{-1} at pH 5 for Pb(II) and pH 4 for Cr(VI). The obtained results revealed that the adsorption efficiency and adsorption capacity showed an inverse relationship with the LS-GO-PANI nanocomposite dose. The maximum adsorption efficiency, 99.7% for Pb(II) and Cr(VI), was achieved with 0.4 g L^{-1} LS-GO-PANI dosage for Pb(II) and Cr(VI), respectively (Figure 10).

Effect of pH and ionic strength effect on adsorption

The effects of solution pH on the accumulation removal of Pb(II) and Cr(VI) onto LS-GO-PANI nanocomposite were studied by varying the aqueous solution pH (Figure 8d). The adsorption of

Pb(II) rapidly increased from pH 2.0 to 3.0, then slowly increased and reached maximum adsorption percentage at pH 4.0 to 5.0 for Pb(II). While the adsorption of Cr(VI) was not rapidly increased from pH 2.0 to 3.0, then slowly increased and reached maximum adsorption percentage at pH 4.0 for Cr(VI). At lower pH, the high H^+ concentration was competitive with both metal ions that caused low adsorption. As the solution pH increased, the adsorption of metal ions on the LS-GO-PANI nanocomposite increased due to the decreasing H^+ ion concentration which acted as a competitor to the positive metal ions for adsorption sites on the surface of the nanocomposites. Moreover, adsorption experiments were not studied above pH 6.0 where the metal ions started to precipitate as their hydroxide complexes in aqueous solutions. Therefore, further adsorption studies of both metal ions, Pb(II) and Cr(VI), were studied at pH 5.0 and pH 4.0, respectively. The effect of ionic strength on the adsorption of both metal ions onto LS-GO-PANI nanocomposite was studied using NaCl, KCl, and MgCl_2 as background electrolytes ranging from 0.0 to 0.5 mg L^{-1} . From our results, it was clearly observed that there were no significant changes that occurred in the adsorption of Pb(II) (10 mg L^{-1}) and Cr(VI) (10 mg L^{-1}) onto LS-GO-PANI nanocomposite with the increase of the background ionic strength.

Evaluation of metal ions uptake characteristics of LGPH nanocomposite by the adsorption isotherms

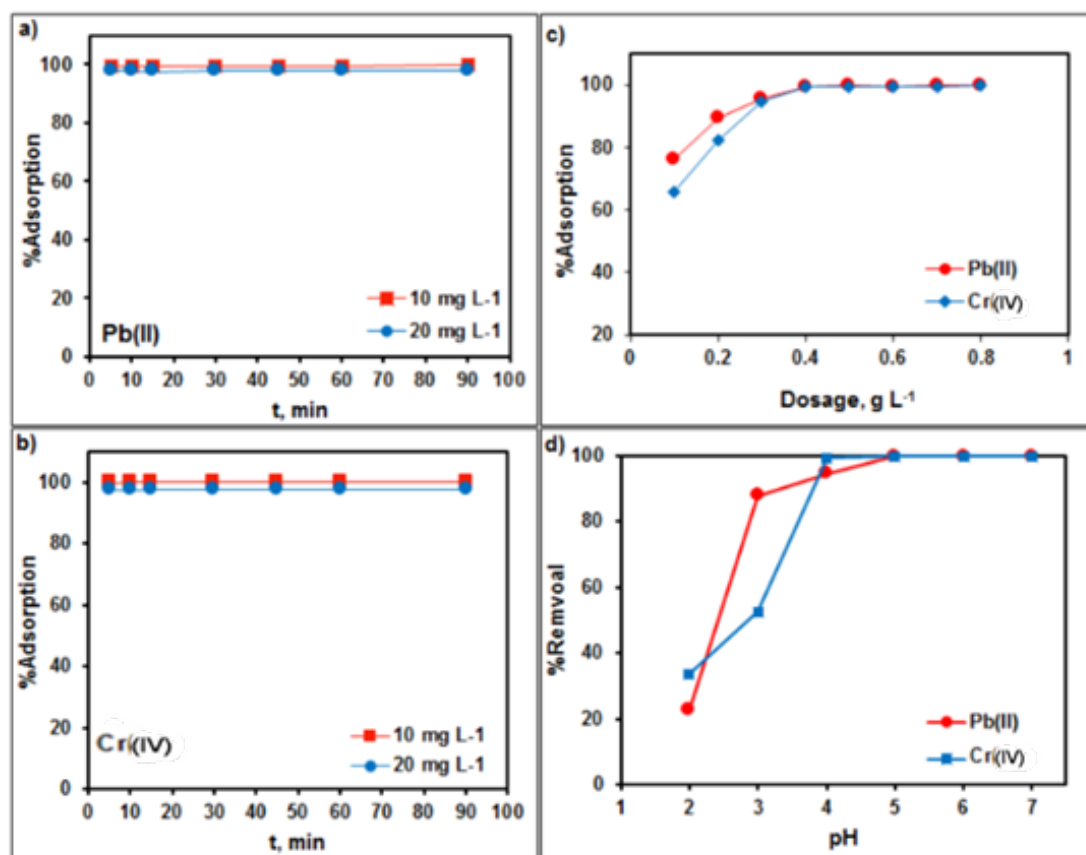


Figure 10: Factors such as equilibrium time (a,b), LS-GO-PANI nanocomposite dosage (c), and aqueous solution pH (d) effect on the adsorption of Pb(II) and Cr(VI) onto LS-GO-PANI nanocomposite at $298 \pm 2 \text{ K}$.

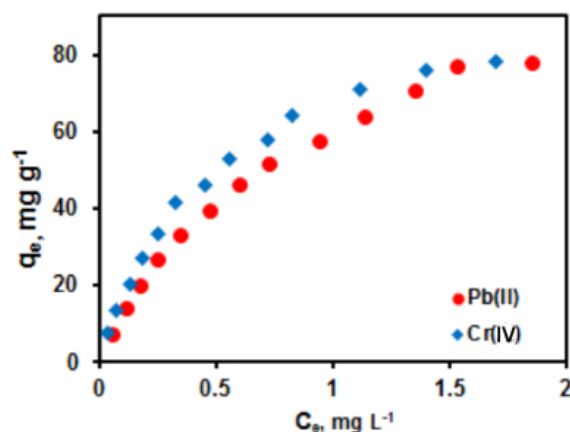


Figure 11: Adsorption isotherms of Pb(II) and Cr(VI) ($C_0 = 2.0$ to 25.0 mg L^{-1}) onto LS-GO-PANI nanocomposite at pH 5.0 for Pb(II) and pH 4.0 for Cr(VI), at 30 min equilibrium time for the range of reaction temperatures, $298\text{--}328 \pm 2.0$ K.

After finding the optimum time, dosage, and pH of the metal ions, adsorption isotherm experiments were performed for the evaluation of the metal uptake mechanism and capacity. Various adsorption models such as Langmuir, Freundlich, and Tempkin were used for the experimental isotherms data as shown in Figure 11. The calculated isotherm parameters, correlation coefficient (R^2) values, and standard deviations in the measurement were used for the evaluation of the suitability of the isotherms and are summarized in Table 1. The Langmuir adsorption isotherm data fit well with the experimental adsorption data compared to the other two models. The adsorption parameters are summarized in Table 1. Hence, the adsorption of Pb(II) and Cr(VI) onto LS-GO-PANI nanocomposite was a monolayer chemisorption on the homogeneous surface. The adsorption capacity of LS-GO-PANI nanocomposite was greater than that of GO alone due to the high electron transfer charge of LGPH nanocomposite by LS. The maximum adsorption capacity of LGPH nanocomposite at 298 ± 2 K for Pb(II) and Cr(VI)

was high, indicating LS-GO-PANI nanocomposite to be a promising and better adsorbent for heavy metal adsorption. It was also clearly observed from Table 1 that the adsorption capacity of LS-GO-PANI nanocomposite was higher than the GO indicates the synergistic enhancement of the adsorption metal ion onto LGPH nanocomposite. The high adsorption of LS-GO-PANI nanocomposite may be due to the fact that the LS-GO-PANI nanocomposite has a high surface area and high surface site density when compared with GO. The distribution of Pb(II) and Cr(VI) between the LGPH nanocomposite in equilibrium over a range of concentrations at three different temperatures ($298\text{--}328$ K) was studied. From the Langmuir isotherm model, the calculated maximum adsorption capacities (q_{max}) were increased as the temperature increased from 298 to 328 K for both metal ions. The increasing adsorption capacity with increasing temperature is associated with endothermic adsorption of metal ions onto LS-GO-PANI nanocomposite at equilibrium. Hence, the adsorption process was favorable and rapid (Figure 11 & Table 1).

Table 1: Isotherm parameters of Pb(II) and Cr(VI) ($C_0 = 2.0$ to 25 $\text{mg} \cdot \text{L}^{-1}$) adsorption onto LS-GO-PANI nanocomposite at 0.4 $\text{g} \cdot \text{L}^{-1}$ dosage and 298 ± 2 K for 30 min ($n = 3$, mean).

Ion	Composite	Langmuir			Freundlich			Temkin		
		qm(mg/g)	KL(L/mg)	R^2	KF(mg/g)	n	R^2	KT(L/mg)n	B	R^2
Pb(II)	LS-GO-PANI	356.4	1.85	0.993	69.12	1.42	0.978	25.54	62.51	0.987
Pb(II)	GO	67.35	0.16	0.993	8.81	0.52	0.895	0.84	12.4	0.86
Cr(VI)	LS-GO-PANI	282.15	1.92	0.996	67.82	1.54	0.987	27.4	56.42	0.978
Cr(VI)	GO	58.52	0.89	0.992	10.89	0.301	0.88	2.84	13.25	0.921

Conclusion

A green novel approach to synthesis lignosulfonate-graphene oxide-polyaniline (LS-GO-PANI) porous hydrogel nanocomposite via solvothermal route and further investigated for the adsorptive removal of lead ions Pb(II) and chromate ions Cr(VI) from aqueous solution. The modification of graphene composite with lignosulfonate (LS) improved its adsorption sites, resulting in excellent Cr(VI) accumulation efficiency from aqueous solution Kinetic and

isotherm studies revealed that pseudo-second-order and Langmuir models, respectively. The adsorption capacity of LGPH nanocomposite for Pb(II) ions was found to be 356.4 mg/g . In case of Cr(VI) ions, LS-GO-PANI nanocomposite exhibited adsorption capacity of 282.15 mg/g . Thermodynamic analysis suggested that the adsorption was spontaneous and endothermic in nature. Lead adsorption was found to be low at acidic pH, and reached a maximum at pH 5.0–7.0. Cr(VI) ions adsorption was a maximum at pH 4.0–7.0, and decreased with the increase in pH above 7.

Conflicts of Interest

The authors declare no conflict of interest regarding the publication of this paper.

Acknowledgement

None.

References

- Camizuli E, Scheifler R, Garnier S, Monna F, Losno R, et al. (2018) Trace metals from historical mining sites and past metallurgical activity remain bioavailable to wildlife today. *Sci Rep* 8: 3436-3440.
- Hansson SV, Grusson Y, Chimienti M, Claustres A, Jean S, et al. (2019) Legacy Pb pollution in the contemporary environment and its potential bioavailability in three mountain catchments. *Sci Total Environ* 671: 1227-1236.
- Wang ZQ, Wu AG, Ciacchi LC, Wei G (2018) Recent advances in nanoporous membranes for water purification. *Nanomaterials* 8: 65.
- Cundy AB, Croudace IW (2017) The fate of contaminants and stable Pb isotopes in a changing estuarine environment: 20 years on. *Environ Sci Technol* 51: 9488-9497.
- Li KT, Wu G H, Wang M, Zhou X H, Wang Z Q (2018) Efficient removal of lead ions from water by a low-cost alginate-melamine hybrid sorbent. *Appl Sci* 8: 1518-1522.
- Li Y, Qiu TB, Xu XY (2013) Preparation of lead-ion imprinted crosslinked electro-spun chitosan nanofiber mats and application in lead ions removal from aqueous solutions. *Eur Polym J* 49: 1487-1494.
- Mohan D., & Pittman C U (2006) Activated carbons and lowcost adsorbents for remediation of tri- and hexavalent chromium from water. *Journal of Hazardous Materials* 137: 762-811.
- Song D, Kaiwen Pan, Akash Tariq, Azizullah Azizullah, Feng Sun, et al. (2016) Adsorptive removal of toxic chromium from waste-Water using wheat straw and Eupatorium adenophorum. *PLOS ONE* 11: e0167037.
- Davis M E (2002) Ordered porous materials for emerging applications. *Nature* 417: 813-821.
- Tyagi A, Tripathi K M, Singh N, Choudhary S, Gupta R K (2016) Green synthesis of carbon quantum dots from lemon peel waste: applications in sensing and photocatalysis. *RSC Advances* 6: 72423-72432.
- Tripathi K M, Tran T S, Kim Y J, Kim T (2017) Green fluorescent onion-like carbon nanoparticles from flaxseed oil for visible light induced photocatalytic applications and label-free detection of Al(III) ions. *ACS Sustainable Chemistry & Engineering* 5: 3982-3992.
- Tripathi KM, Singh A, Bhati A, Sarkar S, Sonkar SK (2016) Sustainable feasibility of the environmental pollutant soot to few-layer photoluminescent graphene nanosheets for multifunctional applications. *ACS Sustainable Chemistry & Engineering* 4: 6399-6408.
- Titirici M M, White R J, Brun N, Budarin VL, Dang Sheng S, et al. (2014) Sustainable carbon materials. *Chem Soc Rev* 44: 250-290.
- Mohan D, Pittman CU (2006) Activated carbons and low cost adsorbents for remediation of tri- and hexavalent chromium from water. *Journal of Hazardous Materials* 137: 762-811.
- Chakraborty A, Deva D, Sharma A, Verma N (2011) Adsorbents based on carbon microfibers and carbon nanofibers for the removal of phenol and lead from water. *J Colloid Interf Sci* 359: 228-239.
- Tao YG, Ye L B, Pan J, Wang Y M, Tang B (200) Removal of Pb(II) from aqueous solution on chitosan/TiO₂ hybrid film. *J Hazard. Mater* 161: 718-722.
- Han Y, Xu Z, Gao C (2013) Ultrathin graphene nanofiltration membrane for water purification. *Adv Funct Mater* 23: 3693-3700.
- Ragnini CAR, Di Iglia RA, Bizzo W, Bertazzoli R (2000) Recycled niobium felt as an efficient three-dimensional electrode for electrolytic metal ion removal. *Water Res* 34: 3269-3276.
- Gao F F, Du X, Hao X G, Li S S, Zheng J L, et al. (2017) A potential-controlled ion pump based on a three-dimensional PPy@GO membrane for separating dilute lead ions from wastewater. *Electrochim. Acta* 236: 434-442.
- Wang Y, Guo L, Qi P F, Liu X M, Wei G (2019) Synthesis of three-dimensional graphene-based hybrid materials for water purification: A review. *Nanomaterials* 9: 1123-1130.
- Abdel-Halim S H, Shehata, A M A, El-Shahat M F (2003) Removal of lead ions from industrial waste water by different types of natural materials. *Water Res* 37: 1678-1683.
- Klapiszewski L, Bartczak P, Wysokowski M, Jankowska M, Kabat K, et al. (2015) Silica conjugated with kraft lignin and its use as a novel 'green' sorbent for hazardous metal ions removal. *Chem Eng J* 260: 684-693.
- Fang R, Tian WM, Chen XBA (2017) Synthesis of injectable alginate hydrogels with muscle-derived stem cells for potential myocardial infarction repair. *Appl Sci* 7: 252-258.
- Judit E, Puskas Ph.D (2013) Introduction to Polymer Chemistry: A Biobased Approach, Technology & Engineering A Biobased Approach: Order Department, DEStech Publications, Inc. 439 North Duke Street Lancaster, PA17602, U.S.A.
- Lakouraj M M, Mojerlou F, Zare E N (2014) Nanogel and superparamagnetic nanocomposite based on sodium alginate for sorption of heavy metal ions. *Carbohydr Polym* 106: 34-41.
- Wang ZQ, Huang YG, Wang M, Wu GH, Geng TM, et al. (2016) Macroporous calcium alginate aerogel as sorbent for Pb²⁺ removal from water media. *J Environ Chem Eng* 4: 3185-3192.
- Godiya CB, Cheng X, Li D W, Chen Z, Lu X L (2019) Carboxymethyl cellulose/polyacrylamide composite hydrogel for cascaded treatment/reuse of heavy metal ions in wastewater. *J Hazard Mater* 364: 28-38.
- Wessling Bernhard (2010) New Insight into Organic Metal Polyaniline Morphology and Structure. *Polymers* 2(4): 786-798.
- Yin Xi, Chung Hoon T, Martinez Ulises Lin L, Artyushkova K, Zelenay Piotr (2019) PGM-Free ORR Catalysts Designed by Templating PANI-Type Polymers Containing Functional Groups with High Affinity to Iron. *Journal of the Electrochemical Society* 166(7): 3240-3245.
- Unnithan MR, Vinod VP, Anirudhan TS (2004) Synthesis, characterization, and application as a chromium (VI) adsorbent of amine-modified polyacrylamide-grafted coconut coir pith. *Ind Eng Chem Res* 43: 2247-2255.
- Pan LH, Wang ZQ, Zhao X Q, He HY (2019) Efficient removal of lead and copper ions from water by enhanced strength-toughness alginate composite fibers. *Int J Biol Macromol* 134: 223-229.
- Wang ZQ, Jin PX, Wang M, Wu GH, Sun JY, et al. (2018) Highly efficient removal of toxic Pb²⁺ from wastewater by an alginate-chitosan hybrid adsorbent. *J Chem Technol Biotechnol* 93: 2691-2700.
- Yang J, Wu JX, Lu QF, Lin TT (2014) Facile preparation of lignosulfonate-graphene oxide-polyaniline ternary nanocomposite as an effective adsorbent for Pb (II) ions. *ACS Sustain Chem Eng* 2: 1203-1211.
- Sprynskyy M, Buszewski B, Terzyk A P, Namiesnik J (2006) Study of the selection mechanism of heavy metal (Pb²⁺, Cu²⁺, Ni²⁺, and Cd²⁺) adsorption on clinoptilolite. *J Colloid Interf Sci* 304: 21-28.
- Acik M, Lee G, Mattevi C, Pirkle A, Wallace RM, et al. (2011) The role of oxygen during thermal reduction of graphene oxide studied by infrared absorption spectroscopy. *J Phys Chem C* 115: 19761-19781.
- Gao X, Jang J, Nagase S (2010) Hydrazine and thermal reduction of graphene Oxide: reaction mechanisms and design. *J Phys Chem C* 114: 832-842
- Kumar PV, Bardhan NM, Chen G, Li Z, Belcher A M, et al. (2016) New insights into the thermal reduction of graphene oxide: impact of oxygen clustering. *Carbon* 100: 90-98.

38. Fernández-Merino MJ, Guardia L, Paredes J I, Villar-Rodil S, Solís-Fernández P, et al. (2010) A review of graphene and graphene oxide sponge: material synthesis and applications to energy and the environment *J Envir Sc C* 114: 6426-6432.
39. Huan J (2006) Syntheses and applications of conducting polymer polyaniline nanofibers *Pure Appl. Chem* 78: 15-27.
40. Bizeto MA, Constantino VRL (2005) Microporous Layered niobate nanosheets: building blocks for advanced materials assembly *Mesoporous Mater* 83: 212-218.